Materials and Design 195 (2020) 109016

Contents lists available at ScienceDirect

Materials and Design

journal homepage: www.elsevier.com/locate/matdes

Nanofatigue behaviour of single struts of cast A356.0 foam: cyclic deformation, nanoindent characteristics and sub-surface microstructure

M. Schmahl [a], A. Märten [a], P. Zaslansky [b], C. Fleck [a,*]

[a] Materials Science & Engineering, Technische Universität Berlin, Straße des 17. Juni 135, 10623 Berlin, Germany
[b] Restorative and Preventive Dentistry, Charité - Universitätsmedizin Berlin, Aßmannshauser Straße 4-6, 14197 Berlin, Germany

HIGHLIGHTS

- Millimetre-sized struts of a cast AlSiMg foam were cyclically nanofatigued up to 10^5 cycles.
- Quasi-static nanoindentation revealed inclusion effects on local properties.
- Silicon inclusions affected cyclic properties at a distance of 5 to 10 μm.
- Nanocyclic deformation behaviour was strongly affected by residual stress release.
- We observed significant hardening for $N \leqq 10^3$. Hardening decreased for $N \geqq 10^4$, sometimes down to saturation.

GRAPHICAL ABSTRACT

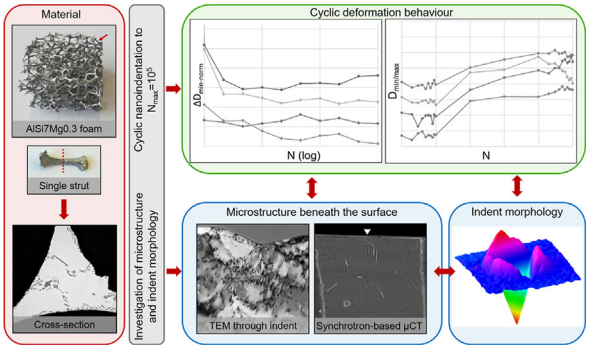

ARTICLE INFO

Article history:
Received 21 October 2019
Received in revised form 27 July 2020
Accepted 28 July 2020
Available online 4 August 2020

Keywords:
Al-Si-Mg alloy
Open-cell metal foam
Nanoindentation
Nano-fatigue
Cyclic deformation behaviour
Phase-contrast enhanced microcomputed tomography (PCE-μCT)
Transmission electron microscopy
Indent morphology

ABSTRACT

Struts are the main load carrying elements in cyclically loaded open cell metal foams. Little is known about the local fatigue behaviour and the influence of the microstructure on nanoscale deformation mechanisms. Different to the bulk counterpart, the millimetre-sized struts in precision-cast AlSi7Mg0.3 foams contain only 1–2 Al-dendrites, Si-Al-eutectic and intermetallic phases. We applied cyclic nanoindentation to $N = 10^5$ to assess nanofatigue. The change in minimum depth per cycle and the ratio of minimum to maximum indentation depths versus the number of cycles correspond to cyclic plastic processes. These and the indent and pile-up morphologies were correlated with the microstructure and dislocation formations revealed by phase-contrast-enhanced micro-computed tomography and transmission electron microscopy. Our results reveal that Si-particles affect deformation within 5 to 10 μm from the indent, and that they favour the formation of fatigue induced dislocation cells in the affected volume. We believe that this interaction is mediated through residual stresses. Furthermore, local variations in microstructure strongly influence the cyclic deformation behaviour and the indent pile-up size and morphology. Interestingly, the results well coincide with observations during fatigue of the bulk alloy reported in the literature.

1. Introduction

Metal foams are a modern class of materials that recently gained increasing interest due to their impressive weight-to-stiffness ratios and excellent damping, insulation and energy absorption properties [1]. They offer design flexibility and make it possible to combine different functions such as load bearing and media storage. They have particularly promising use for applications in weight-restricted fields [2], involving complex quasi-static and cyclic loading conditions. An important route for creating open-cell metal foams is by investment casting, for example of aluminium silicon (AlSi) alloys. Specifically,

* Corresponding author.
E-mail address: claudia.fleck@tu-berlin.de (C. Fleck).

https://doi.org/10.1016/j.matdes.2020.109016

near-eutectic compositions containing magnesium (Mg), e.g. the alloy A356.0 (AlSi7Mg0.3), are easily used for the production of precision cast open-cell metal foams [3].

The macroscopic fatigue behaviour of cast Al-based foams has been widely investigated revealing a large scatter in fatigue life [4–6]. A high scatter is also typical for the quasi-static properties, where it has been assigned to a statistical distribution of defects on the different levels of the hierarchical microstructure [7]. The high scatter means that large numbers of samples must be tested to reliably characterise the fatigue properties. An alternative approach is to focus on the local behaviour of the main load carrying elements. Improved knowledge about the cyclic deformation mechanisms of the single struts may serve to better predict foam performance. Microstructural characteristics in the single struts are known to strongly influence the foam behaviour under quasi-static loading conditions [7,8] and are likely to critically influence the fatigue behaviour as well.

Due to a low cooling rate [9], the microstructure of cast struts of Al-Si-Mg foams is significantly different from bulk alloys with a similar composition. Struts of Al-Si-Mg foams, made by a modified investment casting process, are several millimetres long and about 0.5 mm wide, and they usually consist of only one or two dendrites with a fine Al-Si eutectic in the interdendritic spaces. These dendrites have different orientations of the dendrite backbone with respect to the strut axis and the crystallographic orientation of the grain. As the eutectic is arranged in the spaces between the dendrite arms, there is often a higher amount of eutectic towards the outer strut edges as demonstrated by synchrotron-based micro-computed tomography with slight phase-contrast enhancement. Small Mg_2Si precipitates and few, relatively coarse iron-based intermetallic particles (Fe-IMP) are found in the matrix and in the interdendritic spaces [8–10].

For bulk Al-Si-alloys, the fatigue failure mechanisms are influenced by various microstructural features including the composition of the phases, the texture, secondary dendrite arm spacing (SDAS) [11,12] and the presence of precipitates on the sub-micrometre size range [12,13]. For example, Si-, Mg_2Si- and IMP-particles hinder dislocation movement resulting in cyclic hardening [13]. However, little is known about how the strikingly different microstructure of the struts influences the fatigue behaviour. A precise characterisation of the fatigue mechanisms in the strut material is required for successfully predicting the fatigue behaviour of open cell foams. However, the small dimensions of the millimetre-sized struts make fatigue testing extremely difficult. Nanoindentation offers an excellent alternative well suited to investigate the local mechanical properties under cyclic loading conditions of tiny pillar-shaped specimens. To the best of our knowledge, to date, such nanofatigue tests in the high cycle regime have not yet been reported.

Nanoindentation was originally developed to characterise the mechanical properties of thin films [14–16]. Over time, the method has been increasingly used for a much wider range of bulk and porous materials [17–23]. Commonly, nanoindentation is used under one of two measurement regimes: i) quasi-static loading, where hardness and stiffness are calculated from force-depth curves obtained from single, relatively slow indentation events; ii) nano-DMA (dynamic mechanical analysis) tests, assessing loading-rate dependent stiffness, where the loading amplitude is kept constant during frequency sweeps. In nano-DMA tests, the material is indented repeatedly and elastically at the same point. If higher loads are applied repeatedly, material fatigue comes into play. Cyclic nanoindentation with such higher loads may reveal fatigue mechanisms at the micro- and nanoscale. Specifically, this makes it possible to characterise the influence of grain boundaries or second phases on the cyclic deformation behaviour on the nanoscale. Such information augments fatigue measurements performed on the macroscale. Ultimately, such knowledge may establish the basis for mechanism-based predictions of the cyclic deformation behaviour, especially for hierarchically structured materials.

So far, cyclic nanoindentation has mainly been applied to thin films [24,25]. It has rarely been used for assessing the fatigue properties of materials, usually bulk metals [26,27]. Most of the work characterised low cycle fatigue, with cycle numbers below 3×10^3. Nanofatigue tests with cyclic nanoindentation on magnesium [26] and copper [27] focused on the development of depth of the indents with cycle number. For magnesium, crack growth and the influence of a heat treatment on plastic deformation mechanisms, twinning and slipping, were also reported [26]. Interestingly, cyclic micro-indentation with up to 10 cycles was successfully used for fatigue life predictions [28]. Overall, additional information is still needed for better understanding the local fatigue deformation mechanisms on the nano-scale.

Here we report the quasi-static mechanical properties and the fatigue behaviour of single millimetre-sized struts of AlSi7Mg0.3 open-cell foam. Nano-scale structure and mechanical response are evaluated for high cycle fatigue nanoindentation up to 10^5 cycles. The evaluations of changes in indentation depth over the number of cycles show predominantly cyclic hardening. We correlate the results with the geometry of the indents, observed by scanning probe microscopy, and the microstructure around them, characterised in 2D and 3D by phase-contrast enhanced micro-computed tomography and transmission electron microscopy. We identify important influences of the microstructure below the indents on the cyclic deformation behaviour of the strut material.

2. Experimental procedures

2.1. Material and sample preparation

Open-cell A356.0 (7 wt% Si, 0.3 wt% Mg) Al-alloy foams with 10 ppi pore size were fabricated by a modified investment casting process (Foundry Institute, RWTH Aachen, [9]). Single millimetre-sized struts (Fig. 1b) were extracted from the as-cast foam (Fig. 1a) using wire-

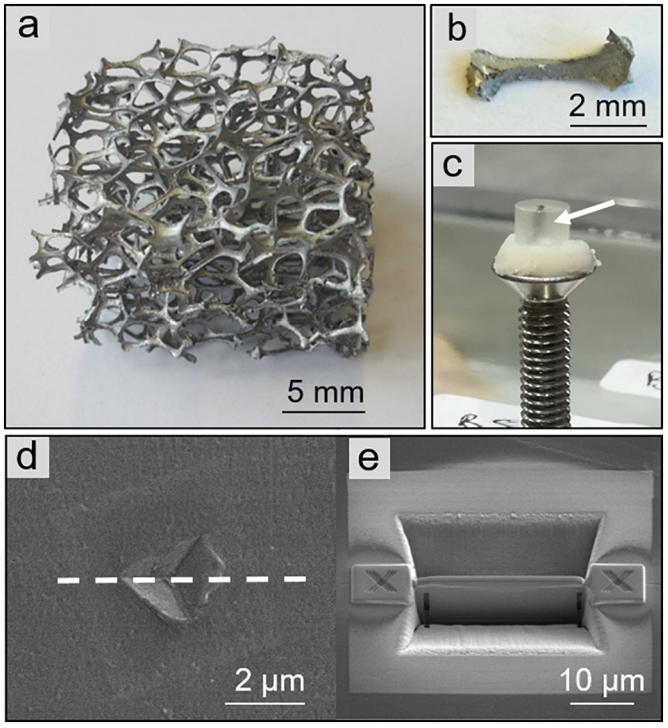

Fig. 1. a) Structure of open-cell Al-Si-Mg foam; b) single strut extracted from the foam structure; c) embedded and indented strut mounted for PCE-µCT (white arrow highlights the strut within the embedding); d) SEM micrograph of one shown indent on a strut cross-section (white dashed line source of TEM lamella in (e)); e) SEM micrograph of FIB extracted TEM lamella cut through the indent tip.

cutting pliers while avoiding shearing or bending of the struts. Fig. 1 shows a typical foam sample and illustrates the specimen preparation steps. To prepare even and smooth cross-sections for nanoindentation, single struts were embedded upright in EpoFix resin (Struers, Ballerup, Denmark) and subsequently ground with a series of silicon carbide papers, polished with diamond suspension down to a grain size of 3 μm and further polished with a colloidal silica slurry with a particle size of 50 nm. For tomographic imaging following nanoindentation, cylindrical samples were drilled out of the polished blocks each containing one strut (Fig. 1c). For transmission electron microscopy (TEM) 100 nm thick lamellae were milled within longitudinal sections cut through the tip of the indent with a focused ion beam (FIB) (Fig. 1 d) (FEI Helios NanoLab 600, Field Electron and Ion Company, Hillsboro, USA) using a gallium ion beam. To ensure positioning through the indent tip during thinning, nano-markers were first milled around the indent. The specimen surface was covered with a thin layer of platinum to protect it from the gallium ions. In this manner we were able to obtain TEM samples without any plastic deformation from sample preparation.

2.2. Quasi-static nanoindentation

The mechanical properties of the Al-matrix and the eutectic Si were determined by quasi-static nanoindentation tests using a trapezoidal load function in a TI 950 TriboIndenter (Bruker, Billerica, USA) equipped with a Berkovich tip. Several groups of indents were placed (i) in the α-Al-matrix ($n = 300$), (ii) on the Si-particles ($n = 50$), and, (iii) in the α-Al-matrix with increasing surface distances from visible Si-particles employing a constant spacing of 5 μm (n = 50: ten lines with 5 indents each) (Fig. 2). Indent positioning was planned based on observations of the different alloy phases, clearly distinguishable by their appearance following polishing. The distance between indents was at least 2.5 times the size of the indents, mostly 3 μm to 4 μm apart, to avoid mutual interactions. The α-Al-matrix and the Si-particles were loaded with a maximum force of 1000 μN and 5000 μN, respectively. These forces gave sufficient indentation depths for reproducible determination of hardness and reduced elastic modulus values. The maximum load was held for 5 s before unloading to 0 μN. The loading and unloading rates were 200 μN/s and 1000 μN/s, respectively. Hardness and reduced elastic modulus were calculated from the load-displacement curves according to the standard method described by Oliver and Pharr [29,30].

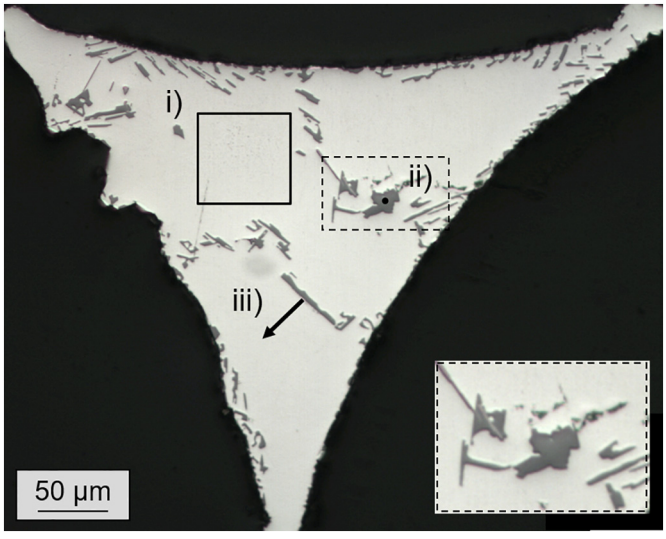

Fig. 2. Ground and polished cross-section of an A356.0 open-cell foam strut: phases appearing white and grey are α-Al and Si-particles, respectively. Quasi-static nanoindentation was performed i) as maps in the α-Al-matrix (marked by a rectangle), ii) on the Si-particles (marked by black dot), and iii) as line-scans in the α-Al-matrix with increasing lateral distance from a Si-particle. Dashed rectangle is a magnified view of the eutectic in region (ii).

2.3. Nanoscale fatigue testing

The nano-scale fatigue behaviour was investigated by cyclic nanoindentation with closed-loop force control and a frequency of 201 Hz up to a maximum number of cycles of 10^5. During such relatively fast "loading" cycles, it is not possible to acquire sufficient data to evaluate full load-displacement hysteresis loops. Therefore, fast loading was interrupted after every 10^{th}, 100^{th}, 1000^{th} and $10{,}000^{th}$ cycle, to perform several ($n = 3$) slow cycles with a loading frequency of 0.1 Hz, also with closed-loop force control. These slow indents were used as nanoindentation "measurement cycles".

Two loading regimes were chosen: during slow and fast loading, the maximum and the minimum forces were $P_{max} = 965$ μN and $P_{min} = 75$ μN ($\Delta P = 890$ μN) in the first case (indents marked with 4-x labels). In the second case, they were $P_{max} = 930$ μN and $P_{min} = 120$ μN ($\Delta P = 810$ μN: indents marked with 5-x and 7–4 labels). The minimum load chosen ensured a constant contact between the tip and the sample surface. The load function is displayed in Suppl. Fig. 1. A settle time of 2 h was used prior to each indentation experiment to minimise thermal drift. The α-Al was indented: (i) in the matrix, far from Si or IMP on the surface, (ii) in the matrix near the eutectic, and (iii) within the eutectic. Indents were placed in 6 struts yielding a total of 14 nanofatigue tests.

2.4. Microstructural and morphological characterisation

The indents and the surrounding surfaces were imaged using the scanning probe microscopy (SPM) mode of the nanoindenter. Both topography and gradient images were evaluated qualitatively and quantitatively with Gwyddion [31] and Fiji [32,33]. The projected area and the outer pile-up area were measured for each of the indents using Fiji where the best fit for both areas was found by visual inspection. Fig. 3 shows a typical SPM topography image result of a cyclic indent and indicates the definitions of these areas. The pile-up volume was determined by integration of all pixels under the area. Indent and pile-up profiles were measured using Gwyddion.

High resolution synchrotron based phase contrast enhanced microcomputed tomography (PCE-μCT) was used to evaluate the microstructure in the entire volumes of the struts. Scans with effective pixel resolutions of 438 nm or 876 nm were obtained using an energy of 30 keV on BAMline, the X-ray imaging beamline of the BESSY II electron storage ring of the Helmholtz Center of Materials and Energy (HZB, Berlin). The cylindrical specimens (Fig. 1 c) were mounted upright using a sample to detector distance of 35 mm to induce moderate phase-contrast enhancement. The data obtained from a PCO-4000 camera mounted on an Optique-Peter imaging system was normalised using customised code, reconstructed with the software NRecon, visualised using CTVox (Bruker-microCT, Kontich, Belgium) and further processed using Fiji.

For higher resolution characterisation of the microstructure and the dislocations below the indents, TEM was performed using an FEI Tecnai G^2 20 S-TWIN (Field Electron and Ion Company, Hillsboro, USA), equipped with an LaB_6 cathode and an accelerating voltage of 200 kV.

3. Results

3.1. Morphological characteristics

3.1.1. Surface roughness

The topography of the samples was mapped by SPM mode of the indenter, in areas surrounding each of the indents (Table 1) and in zones unaffected by mechanical loading. The average roughness ranges from 1.9 nm for the smoothest specimen to 4.3 nm for the roughest surface.

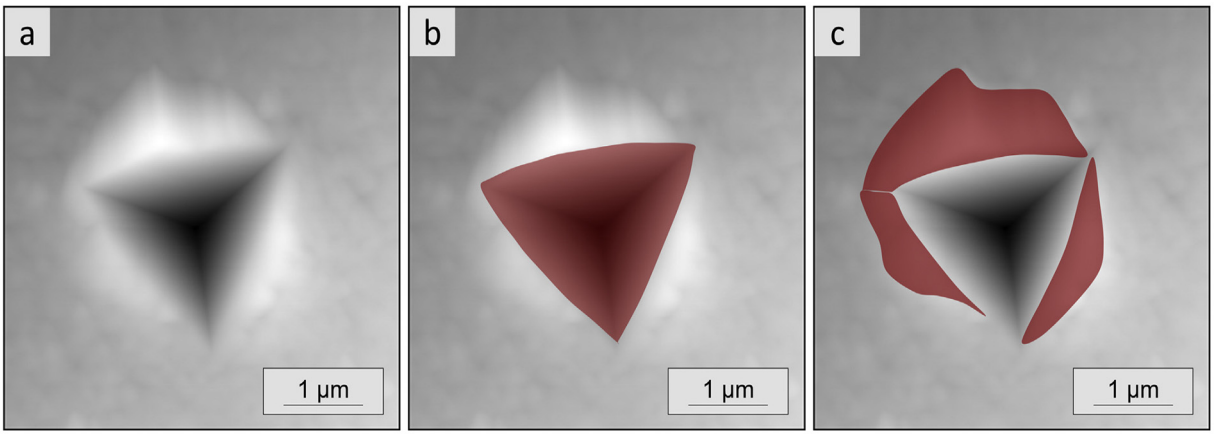

Fig. 3. Evaluation of indent morphological features: a) SPM topography image of a typical cyclic indent; b) typical mask of indent area; c) typical mask of pile-up area.

Such variation was observed both between struts and within the same struts, regardless of which struts were polished together.

3.1.2. Reference, standard nanoindentation ("quasi-static indentation")

Nanoindentation (single cycle) in the α-Al-matrix resulted in prominent indentation marks remaining clearly visible after unloading (Fig. 4). These differed markedly from indents in Si that were barely visible after unloading (data not shown). The indents in the α-Al-matrix presented a range of sizes, with some showing pronounced pile-up while others exhibiting only faint bulging (Fig. 4a-c). Indents with increasing distances from visible Si-particles demarcated the region of possible influence of the harder Si-particles on the nanoindentation behaviour of the Al-matrix (Fig. 2 iii). No visible differences in indent or pile-up size and morphology could be identified with increasing distance.

3.1.3. Cyclic nanoindentation

Fatigue induced indent morphologies are profoundly different from quasi-static indents. Indentation depths and sizes of the pile-up are much higher, and most indents show steps in the pile-up and/or on the faces of the indents. Typical differences between a quasi-static and two typical cyclic nanoindents are presented in Fig. 5.

Table 1
Results of the quantitative analysis of indent and pile-up size and morphology: average roughness (R_a) of the non-deformed surface surrounding the indent, maximum indentation depth after fatigue loading (D_{max} ($N = 10^5$)), projected indent area (A_p), pile-up area ($A_{p\text{-}u}$), pile-up volume ($V_{p\text{-}u}$) and maximum pile-up height ($h_{p\text{-}u,\,max}$).

Indent	Surface	Indent		Pile-up		
	R_a	$D_{max}(N = 10^5)$	A_p	$A_{p\text{-}u}$	$V_{p\text{-}u}$	$h_{p\text{-}u,max}$
	(nm)	(nm)	(μm^2)	(μm^2)	(μm^3)	(nm)
4-1 a	2.71 ± 0.69	218.88	1.767	2.836	0.129	66.9
4-2 a	2.86 ± 0.62	223.45	1.683	1.902	0.045	46.0
4-2 b	2.86 ± 0.69	222.25	1.720	1.632	0.048	48.2
4-2 d	4.01 ± 0.42	208.02	2.262	3.088	0.105	75.0
4-3 a	2.52 ± 0.28	284.33	2.095	1.988	0.065	58.3
4-3 b	3.87 ± 0.62	259.83	2.112	1.942	0.063	76.8
4-3 c	3.17 ± 0.61	278.84	2.309	2.225	0.075	83.4
4-3 d	4.17 ± 1.72	314.46	3.254	2.838	0.140	107.9
4-3 e	3.30 ± 0.16	319.59	4.082	3.952	0.201	149.6
5-1 a	2.25 ± 0.85	250.06	2.879	3.066	0.131	116.2
5-1 d	1.89 ± 0.64	219.66	1.960	1.869	0.074	100.1
5-3 a	4.25 ± 0.78	284.46	2.966	2.896	0.125	160.7
5-3 d	2.94 ± 0.47	272.95	2.576	2.516	0.095	110.9
7-4 c	2.77 ± 1.05	341.46	3.074	3.351	0.134	143.8

The maximum indentation depth in the first cycle (for maximum load) scales with the applied load: the average value for samples loaded with a maximum force of 965 μN was 179 nm ± 13 nm whereas the value for samples loaded to 930 μN was 159 nm ± 10 nm. After cyclic loading, there was no correlation between the applied force and the indentation depth, highlighting the strong influence of the underlying microstructure, as will be shown below.

Fatigue indents were clustered into 5 groups based on indent size, the presence and the size of pile-up, and the presence and the size of steps in the pile-up and/or on the faces of the indents (Fig. 6 & Table 2):

- "type S": **s**mall indent size, only minor pile-up,
- "type M": **m**edium indent size, slightly more pile-up with steps on one side of the indent,
- "type L": **l**arge indent size, large pile-up with steps on one side of the indent, steps on at least one face of the indent, position of the step correlates with partial pile-up at the edge of the indent,
- "type P": very **p**ronounced pile-up with steps on one side of the indent and partial pile-up on the other sides, but no steps on the faces of the indent, and very large indent size,
- "type C": **c**ompound group of individual, non-recurring indent shapes: a) steps visible on the faces of the indent, irregular, pyramidal pile-up on all sides of the indent. b) non-symmetric elongated indent with partial pile-up at one end of the indent.

The maximum pile-up point and the dimensions of the steps were obtained from profiles measured in topography images of the indents as shown in Suppl. Fig. 2. The steps in the pile-up are 100 to 300 nm wide and 5 to 15 nm high, as compared with 30–40 nm height for steps across the entire inside in the indent faces. Table 1 lists the maximum indentation depth, the projected area and the outer pile-up area, for each of the indents, determined by quantitative image analysis. The pile-up areas span 1.63 μm^2 to 3.95 μm^2 and the volumes span 0.045 μm^3 to 0.14 μm^3. The values correlate with the projected area of the indent. The pile-ups are not uniformly distributed along the edges of the indents (best seen in indents of types L and P), and some contain significant local maxima. The linear correlation between the maximum indentation depth after cyclic loading $D_{max}(N = 10^5)$ and the projected area was $R = 0.81$ for indents with hardly any pile-up (type S), and $R = 0.61$ for indents with significant pile-up.

3.2. Microstructure beneath the indents in 3D

To better understand the influence of the microstructure on the nanofatigue behaviour, high resolution PCE-μCT was used. Fig. 7 shows examples of the four types of microstructures that we observed

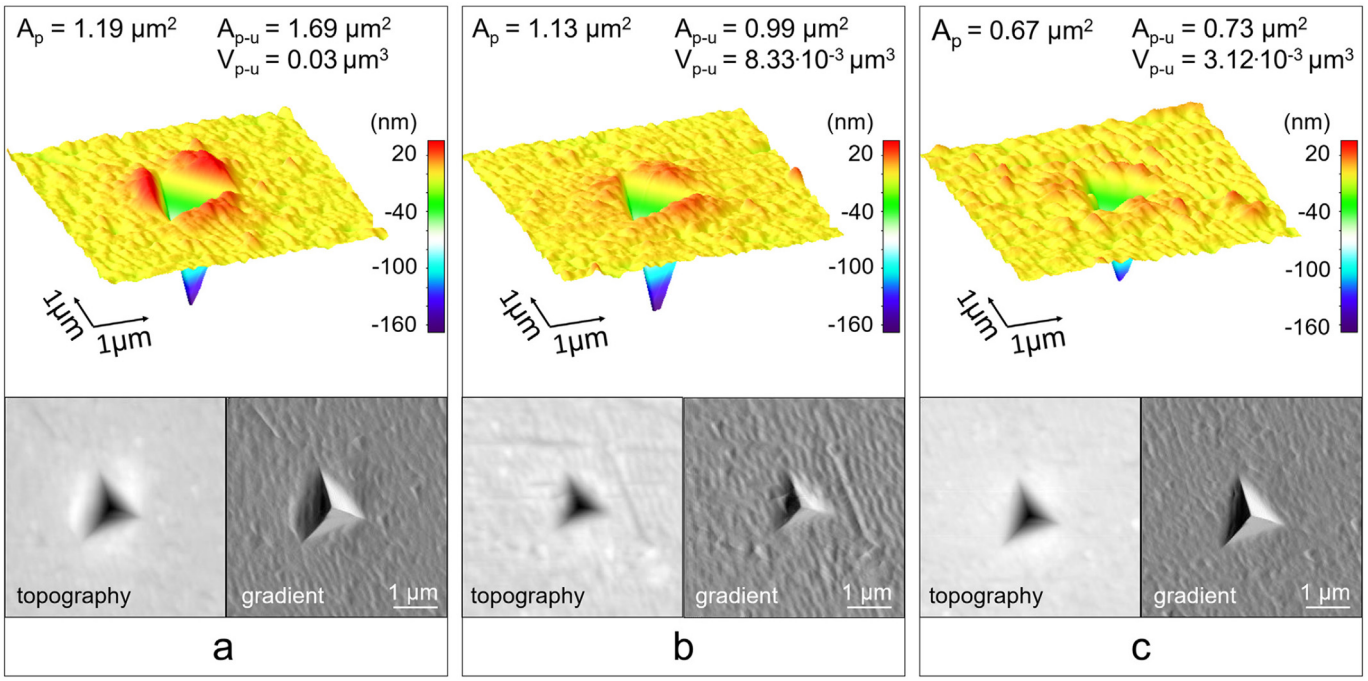

Fig. 4. Results for quasi-static nanoindentation, showing 3 different quasi-static impressions with different indent morphologies. SPM gradient and topography images and 3D surface plots are displayed. a) Larger indent with pronounced pile-up; b) larger indent without significant pile-up; c) small indent without pile-up. The projected area of the indents (A_p), the pile-up area (A_{p-u}) and the pile-up volume (V_{p-u}) were determined after background subtraction. Note different scale of the z-axis (depth of the indent) as compared to the lateral scale, chosen for better visibility of the indent in the 3D surface plots.

in the volumes beneath all cyclic nanoindents. The α-Al-matrix appears grey. The Si-particles appear slightly darker and only become visible due to the phase contrast enhancement induced during imaging. The Fe-IMPs strongly attenuate the X-ray beams and thus appear very bright. Both sections through the data and projections of maximum and minimum intensity in the 3D data are shown. The indents are not visible at this resolution and their approximate position is indicated by the dotted white line, identified on the upper surface position by the white arrowheads. Si-particles are best seen by projection of the minimum intensity through ~80 µm thickness sub-volumes in the tomographic data beneath the indent. Correspondingly, the projections of the maximum intensity highlight the IMPs. The results are summarised in Table 2. We discriminated the microstructures according to their appearance of different phases in a volume of a maximum radius of 10 µm around the indent according to:

- "type Al" lacks any secondary phases in the α-Al-matrix,
- "type Si" contains few particles in the proximity of the indent,
- "type Eu" is characterised by a high concentration of Si-particles, usually a eutectic volume,
- "type IMP" contains IMP-particles, relatively large inclusions near the indent.

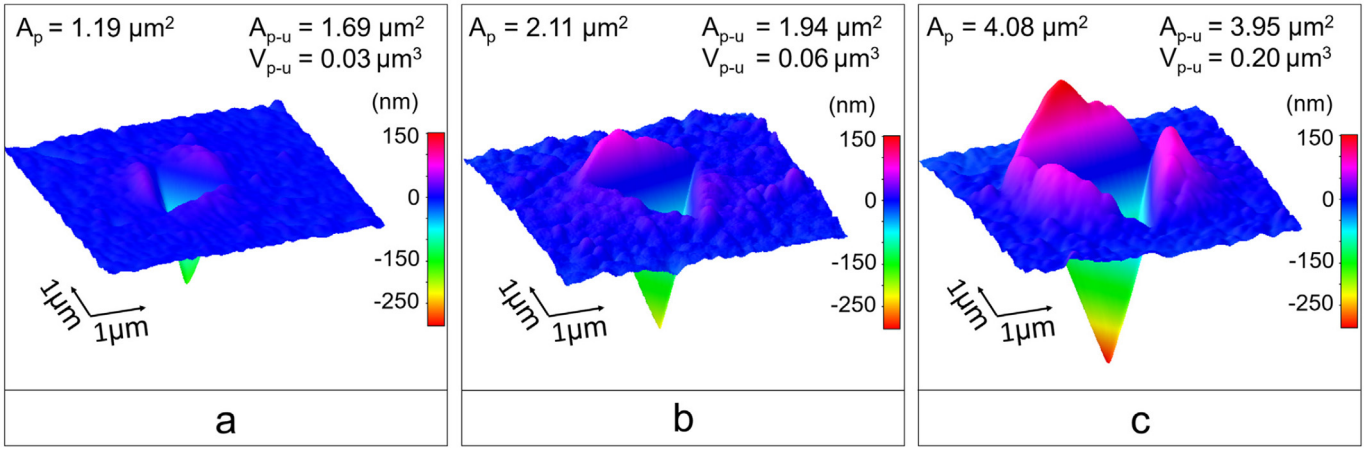

Fig. 5. 3D comparison of the indents of quasi-static and cyclic indentation in the α-Al-matrix. a) Quasi-static indent with pronounced pile-up compared to other typical quasi-static results; b) cyclic indent typical for moderate pile-up; c) cyclic indent typical for increased pile-up and indentation depth. Note that the projected area and the pile-up volume are higher for the cyclic indents compared to the quasi-static indent. The projected area of the indents (A_p), the pile-up area (A_{p-u}) and the pile-up volume (V_{p-u}) were determined after background subtraction. Note different scale of the z-axis (depth of the indent) as compared to the lateral scale.

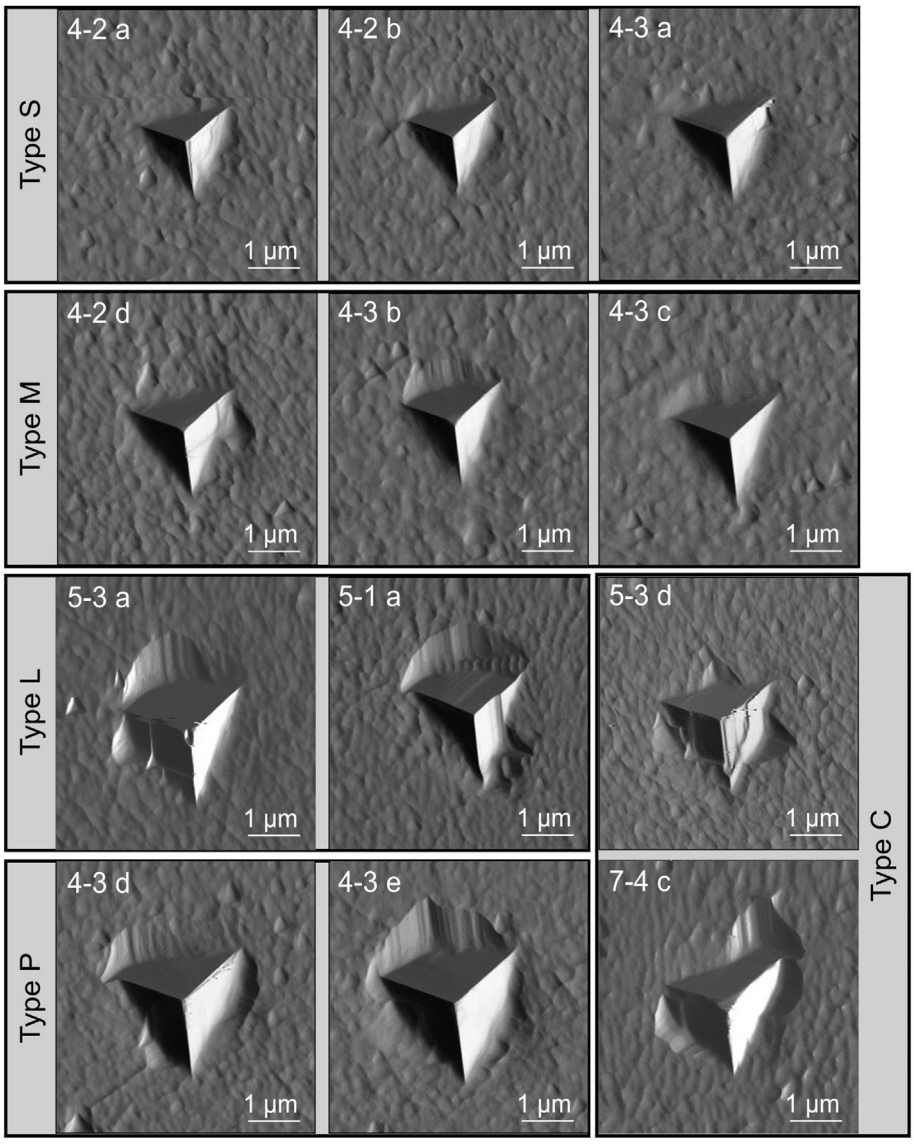

Fig. 6. SPM gradient images of 12 cyclic nanoindents, grouped according to indent size, presence and size of pile-up, and presence and size of steps, visible in the pile-up and/or at the indent faces: type S - small indents with only small pile-up; type M - medium indents with more pile-up and slight steps; type L - large indents with significant pile-up and pronounced steps within the pile-up and on the indent faces; type P - large indents with significant pile-up and steps in the pile-up, but no steps on the indent faces; type C - compound group: relatively small indent with pronounced pile-up and steps (5-3 d); large, irregular indent with significant pile-up and steps (7-4 c).

3.3. Dislocation structure beneath the indents

TEM observations of a non-deformed reference sample (Fig. 8a) show a relatively homogeneous microstructure below the surface. The α-Al-matrix is occasionally interrupted by dislocations (straight dark lines or points). Selected area electron diffraction (SAED) revealed the presence of a single dendrite. The light grey needles (indicated by white arrows) are Si-particles. EDX revealed a low amount of Mg, indicating the additional presence of Mg_2Si. Near the surface, some artefacts developed presumably due to the FIB preparation process.

For quasi-static indents placed in the α-Al-matrix, TEM observations show the microstructure and dislocation density in the volumes below the indents. The indent shown in Fig. 8b, c extends about 200 nm deep. SAED confirmed that a single α-Al dendrite is present (data not shown) with an almost homogeneous microstructure. Only few small needle-shaped precipitates are visible consisting of Si and Mg, as identified by EDX. A higher dislocation density is seen in the volume directly below and around the indent, as compared to the less mechanically affected volume of the specimen, seen in the lower area of the image. The dislocation motion into the deeper volume of the sample appears to have been arrested by a horizontally oriented Si-particle located about 400 nm beneath the indent.

Note that, although we cannot be sure that our TEM lamellae are cut right through the tip, we are certain that they pass very close to it, given that the depth of the observed triangular profile of the indent matches the range of typical indent depths in our study (160 to 200 nm).

TEM measurements of specimens cyclically loaded to 965 µN revealed the microstructure beneath the loaded surface and its relation to the nano-scale fatigue and deformation mechanisms. Fig. 9 shows TEM longitudinal slices from six of the cyclic indents, representing the different indent and microstructural types (Table 2). Indents appear as triangular structures visible at the upper rim of the lamellae. The main differences visible for the different samples are the dislocation density and sub grain structures. In the lamella of indent 4–3 d, the overall

Table 2
Results of the microstructural investigations: for each indent, the groups according to indent size and morphology and to PCE-μCT results of the volumes beneath the indents are listed. For the indents where TEM has been performed, short descriptions and the groups, based on differences in microstructure and dislocation formations, are given.

Indent	Size/morphology (Fig. 6)	PCE-μCT (Fig. 7)	TEM (Fig. 9)
4-1 a	M	Si - Eu	–
4-2 a	S	Al	–
4-2 b	S	Al	–
4-2 d	M	Eu	II: medium-size affected area, pronounced sub grain structures
4-3 a	S	Si	I: small affected area, few indistinct sub grain boundaries
4-3 b	M	Si	III: large affected area, very fine and very pronounced sub grain structure; Si particle near indent
4-3 c	M	Si - Eu	II: medium-size affected area, pronounced sub grain structures
4-3 d	P	IMP	I: small affected area with few indistinct sub grain boundaries
4-3 e	P	Eu	dendrite border: left dendrite II: medium-size affected area, pronounced sub grain structures; right dendrite: single dislocations
5-1 a	L	Al	–
5-1 d	M	Eu	–
5-3 a	L	Al	–
5-3 d	C: M indent & pile-up, pronounced steps	Eu	–
7-4 c	C: elongated indent, medium pile-up, steps	IMP	–

Indent size/morphology groups: S: small indent & pile-up; M: medium indent & pile-up, steps; L: large indent & pile-up, many steps; P: very large indent & pronounced pile-up; steps; C: compound group; PCE-μCT microstructural groups: Eu = eutectic; Al = Al matrix; Si = silicon; IMP = Fe-IMP inclusion.

lowest dislocation density is shown. We observe a few single dislocations (marked by arrow ① in Fig. 9) and some formation of sub grain structures (marked by arrow ② in Fig. 9), limited to the faces of the indent, and only rather indistinct sub grain boundaries. The dotted white arrow without number indicates an artefact caused by the FIB preparation process. The observations in the volume influenced by the indentation process for indent 4–3 a are very similar to 4–3 d, with a slightly higher overall dislocation density. Arrays of parallel, unidirectional dislocations (marked by arrow ① in Fig. 9) are homogeneously distributed throughout the field of view. In a small volume directly beneath the indent and extending across the width of the indent face, the dislocations are clustered, forming two clearly visible sub grains (marked by arrow ② in Fig. 9). Some diffraction artefacts caused by the bending of the lamellae during the FIB preparation process are seen (marked by white arrows without number in Fig. 9). Elemental mapping (Fig. 10 a) showed a higher oxygen content at the surface as compared to the bulk of the specimens which we attribute to the natural formation of an oxide layer.

Indents 4–3 c and 4–2 d are examples for a less homogeneous dislocation structure and more clearly developed sub grains. More extended sub grain structures are visible in a larger volume beneath the indents and the sub grain boundaries are further developed as compared to the indents 4–3 a and 4–3 c. Indent 4–3 b shows a very fine and well-developed sub grain structure. SAED in the areas between the sub grain boundaries (positions marked by * and # in Fig. 9) revealed an orientation difference between these areas, proving that the features we see are indeed sub grains (Fig. 10b). In a confined area directly below these sub grains, the dislocation density is lower, while it is higher again towards the lower part of the lamella. Further, a eutectic Si-particle is seen in the vicinity of the indent, which was not visible in the reconstructed PCE-μCT data (marked by arrow ③ in Fig. 9). The corresponding EDX analysis is shown in Fig. 10c.

While all other investigated lamellae contained only one dendrite, the TEM micrographs of indent 4–3 e clearly show a dendrite border (marked by arrow ④ in Fig. 9). Pronounced sub grain structures are seen in the left dendrite, while only single dislocations are visible in the right dendrite. The differences in orientation and dislocation density between the dendrites and the sub grains in the left dendrite are especially well visible by the pronounced contrast in the STEM image (upper image of 4–3 e): the left dendrite appears much brighter with the sub grains visible as darker areas, and the right dendrite appears in relatively uniform, very dark grey.

3.4. Mechanical properties

Typical load-displacement curves from quasi-static nanoindentation tests on the α-Al-matrix and the Si-particles are shown in Suppl. Fig. 3. For testing the Si-particles, the load was increased by a factor of five to achieve the same indentation depth as in the Al-matrix. While the curves for the Al-matrix are smooth, the curves for the Si-particles show the so-called “elbow effect” in the unloading segment. This effect has been previously related to the formation of an amorphous Si-phase [34]. None of the curves show severe load serrations which would indicate a pop-in effect or crack nucleation. The α-Al-matrix exhibits much higher plasticity in comparison with Si, visible from the higher maximum displacements, perfectly matching the morphological observations. The differences in the deformation behaviour of the two phases are also reflected in the measured values of the hardness and the reduced elastic modulus (Table 3). Both are significantly higher for the Si-particles.

By mapping the α-Al-matrix, indents end up with a variety of distances to the Si-particles on the surface. To investigate a possible influence of this variation as well as possible effects of other inclusions such as IMPs, we placed additional indents in the matrix along lines orthogonal to the interfaces and with increasing distances from Si-particles, as indicated in Fig. 2. Close inspection of such indents with the SPM imaging mode of the nanoindenter did not reveal any correlation between the distance, the indent shape and size in the gradient images and the calculated hardness of the material (Table 4). However, the reduced elastic modulus was roughly 15% higher near the Si-particles, observed for measurements obtained within a distance of 5 μm.

For the fatigue investigations, all indentations were performed in the α-Al-matrix, with different surrounding local microstructures. During fatigue loading, hysteresis loops develop and the maximum and minimum depth (D_{max}, D_{min} respectively) reached in every single cycle change gradually. To evaluate the development of the plastic deformation, we analysed the change in D_{min} from cycle to cycle. ΔD_{min} represents the incremental plastic deformation, induced by the application of the force amplitude over the entire history of loading. The change in minimum displacement between consecutive measurement cycles N_{x+1} and N_x is:

$$\Delta D_{min}(N_{x+1}) = D_{min}(N_{x+1}) - D_{min}(N_x) \quad (1)$$

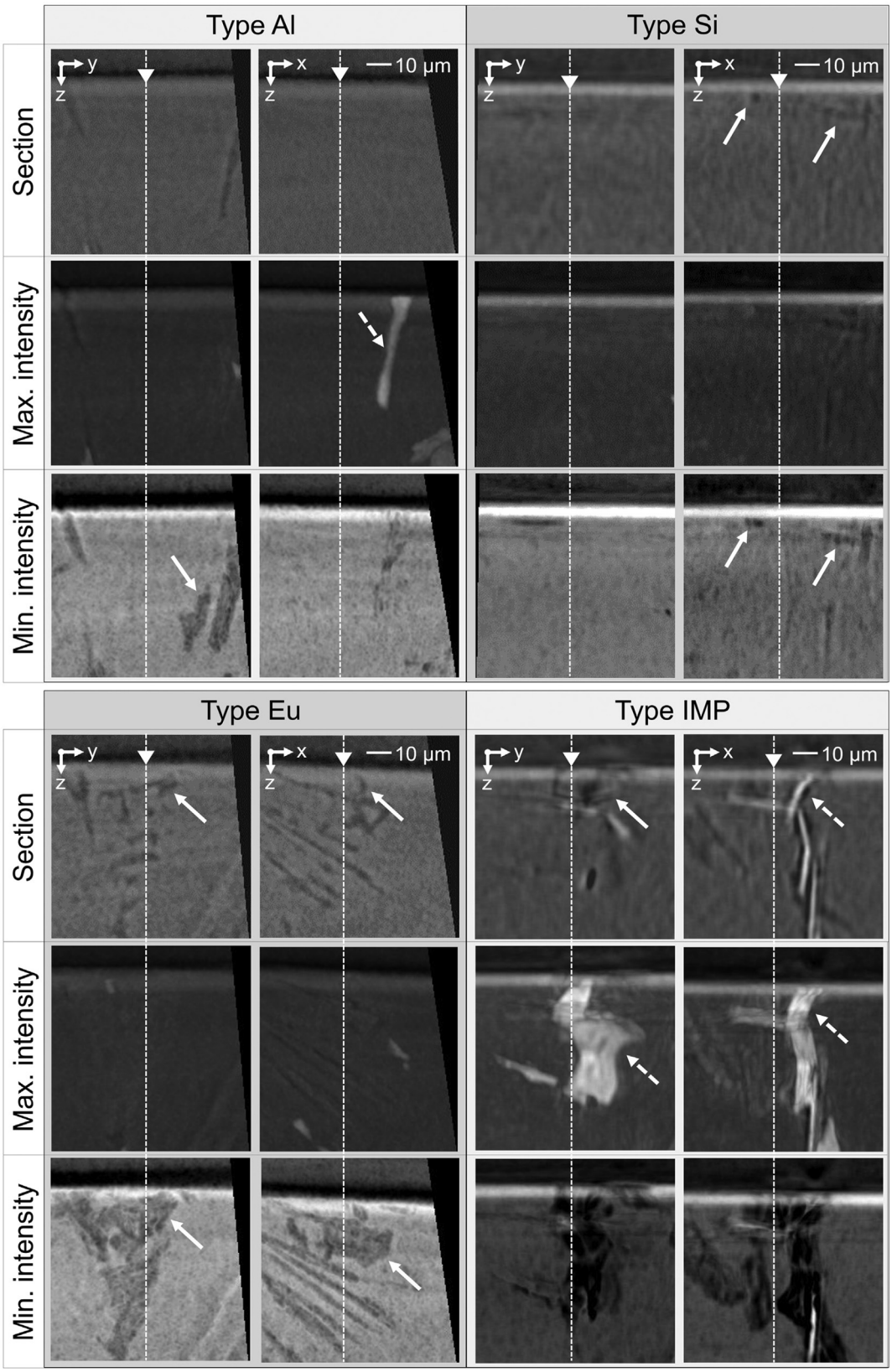

Fig. 7. PCE-µCT data showing typical 3D-microstructures in the volumes below the cyclic nanoindents: distribution of Si-particles and IMPs up to 10 µm beneath the indent: type Al - only α-Al; type Si - some small Si-Mg-particles; type Eu - Si eutectic; type IMP - IMPs and Si-Mg-particles. "Section" denotes longitudinal sections through the reconstructed volumes, max. and min. intensity are projections of the maximum and minimum intensity across 20 µm in the volume beneath the indent. Two orthogonal sections (left and right image) are shown for each type. The white dotted lines and the white arrowhead indicate the indent and surface position. The solid white arrows point to Si-particles which appear in darker grey, and the dotted white arrows point to IMPs which appear in bright grey/white.

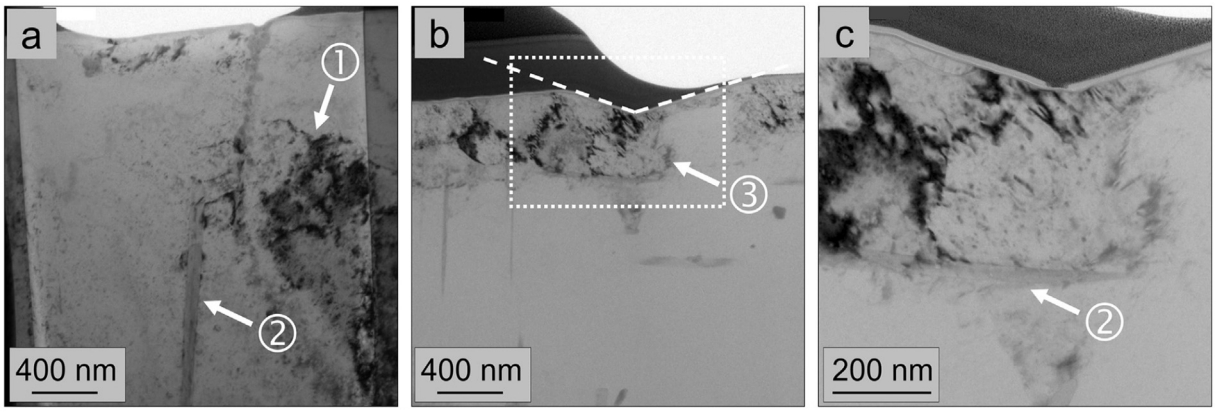

Fig. 8. Bright-field TEM micrographs showing FIB sections through: a) a non-deformed reference sample, and b, c) a quasistatic indent ("triangle", delineated by the dotted line in b). a) The non-deformed state exhibits a very low dislocation density in the α-Al-matrix. Note that the dark areas marked by the black arrow ① are preparation and imaging artefacts as demonstrated by tilting the specimen during TEM observation. An elongated Si-Mg-particle is visible in darker grey (white arrow ②). b, c) Following quasi-static nanoindentation, the dislocation density in the volume below the indent has increased significantly (white arrow ③). With higher magnification (c; area marked in (b) by the white dotted rectangle), a Si-Mg-particle (white arrow ②) is visible, seemingly hindering further dislocation movements into the lower part of the specimen.

and is normalised by the number of cycles over which the change occurred. Since there were slight unavoidable differences in the applied force (~30% in P_{min}) for the different tests, we scale the result by P_{min}:

$$\Delta D_{min-norm}(N_{x+1}) = \Delta D_{min}/((N_{x+1} - N_x) \times P_{min}(N_{x+1})) \quad (2)$$

Fig. 11 shows typical curve progressions for $\Delta D_{min\text{-}norm}$ versus N for two regimes of cycle numbers: up to 10^3, and from 10^4 to 10^5. For the curves of all indents see Suppl. Fig. 4. In the following, we address the first and second regime of cycles as "incipient" and "advanced" fatigue regime.

We see that the changes of plastic deformation are much lower in the advanced regime as compared to the incipient one. All tests show a decrease in the incremental plastic deformation per cycle over N. The variations in $\Delta D_{min\text{-}norm}$ over the first ten cycles and the significantly lower variations during the following cycles are partially due to the averaging performed for the higher cycle numbers, where only every 100^{th}, 1000^{th} or $10{,}000^{th}$ cycles are measured. Different specimens fluctuate differently, suggesting that the changes are also due to a real decrease in the plastic deformation from cycle to cycle, indicating some saturation.

For the incipient regime, two main types of cyclic deformation behaviour are observed (types A1 and A2, see Table 5): the absolute value of the fluctuations during the first ten cycles is more pronounced for the "A2" curves. Furthermore, the "A1" curves exhibit an increase between 10 and 100 cycles followed by a decreasing trend whereas "A2" curves decrease continuously beyond 10 cycles. The curves vary in their incline or decline and many "A2" curves show a lower decline after 10 than after 100 cycles. Some indents are difficult to sort into groups, due to the high variations in the curve progression. For example, indents 4–3 d and 4–3 e, both "A2", show an overall decreasing behaviour after 10 cycles, but the decline between 10 and 100 cycles is very small and almost plateau-like.

With ongoing loading (advanced regime), two main types of behaviour are observed. In the first case (type B1), $\Delta D_{min\text{-}norm}$ is approximately constant on a very low level, indicating a pronounced saturation state. In the second case (type B2), $\Delta D_{min\text{-}norm}$ decreases further up to about 20,000 cycles, followed by a nearly steady state with only slightly decreasing trend. Only three curves (4-1 a, 4-2 a, 4-2 b) show B1 behaviour in the advanced regime, while nearly all other curves exhibit B2 behaviour.

Two curves do not fit the described behaviours: indent 4–2 d exhibits extreme fluctuations of $\Delta D_{min\text{-}norm}$ during the first 10 cycles, with significantly negative values, and a further decrease for the advanced regime with consistently negative changes of $\Delta D_{min\text{-}norm}$, indicating a decrease in the minimum depth over the number of cycles. The second special case is indent 7–4 c where we observe a slight increase in $\Delta D_{min\text{-}norm}$ from 40,000 to 100,000 cycles, indicating continuous softening.

The ratios of D_{min} to D_{max} versus the number of cycles are shown in Fig. 11 and Suppl. Fig. 5. Whereas this value increases if the indented volume behaves increasingly more elastic, it decreases, if a higher amount of plastic deformation occurs or a crack is formed. Here we also observe four different types of behaviour (Table 5): three indents have very similar courses of D_{min}/D_{max} versus N, with a low fluctuation and a clearly visible saturation state following an initial increase in D_{min}/D_{max} up to $N = 100$ (type I). The second group (type II) shows more pronounced fluctuations and a steady increase over N. This increase in D_{min}/D_{max} over N is even more pronounced for the "type III" behaviour. The three remaining specimens exhibit the opposite behaviour (type IV): D_{min}/D_{max} decreases over the last 50,000 to 90,000 cycles, following a range with nearly constant values up to 10 cycles, and an increase afterwards.

4. Discussion

By cyclically indenting up to $N = 10^5$, we were able to induce fatigue characteristics in the Al-matrix of open-cell A356.0 foam struts, similar to those usually seen in bulk Al alloys. The combination of very high resolution localised 2D microstructural analysis (e.g. TEM, Fig. 9) and high resolution 3D analysis of a larger volume (PCE-μCT, Fig. 7), allowed us to develop a comprehensive understanding of the microstructural processes on different length scales. Our results reveal a range of local interactions of the indenter with the microstructure. Significant hardening is observed during the first few cycles, followed by either saturation or further hardening. Local microstructural inhomogeneities, such as Si-particles, influence the matrix behaviour in an interaction volume of 5 to 10 μm. On the nanoscale, we observed typical fatigue induced dislocation structures. The variation in the data suggests that the different indents are in different fatigue states, depending on the secondary phases beneath the area where the force was applied. An important observation was of fluctuations in the cyclic deformation behaviour following repeated loading which we assign to interactions with and the release of residual stresses. Interpretation of our fatigue results requires considering the initial interactions between the indenter and the strut and the changes that evolve over time.

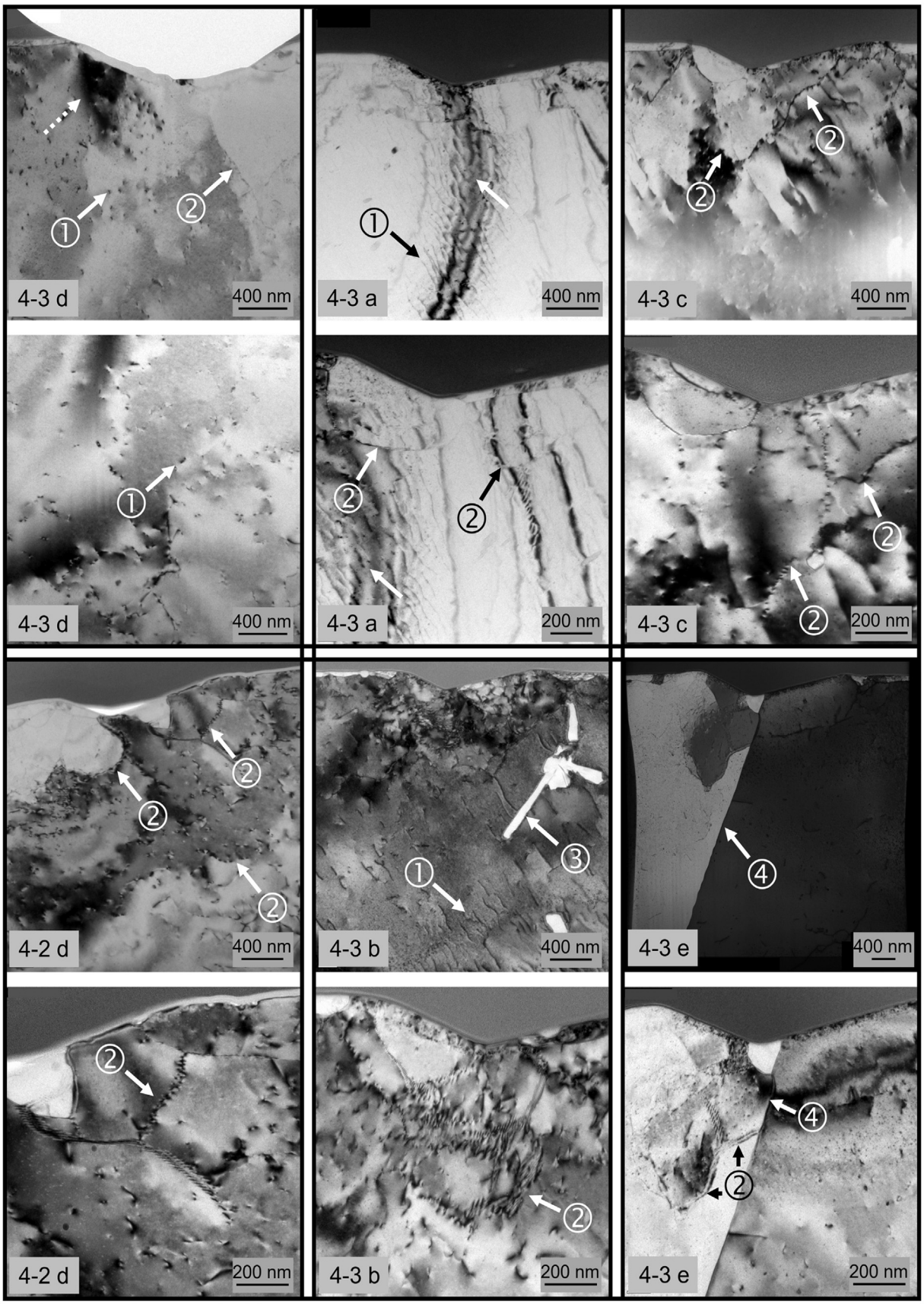

Fig. 9. Typical TEM and STEM images of lamellae prepared through the tips of six cyclic indents. The upper and lower image of each indent show surveys and magnified views, respectively. Microstructural features are indicated by white or black arrows and numbers: dislocations ①, dislocation cells ②, a Si-Mg-particle ③ and a dendrite border ④. SAED was performed on the lamella of indent 4-3 b in two areas next to a sub grain boundary (marked with * and #). The white arrows without numbers in the micrographs of indent 4-3 d and 4-3 a point to preparation and diffraction artefacts, respectively.

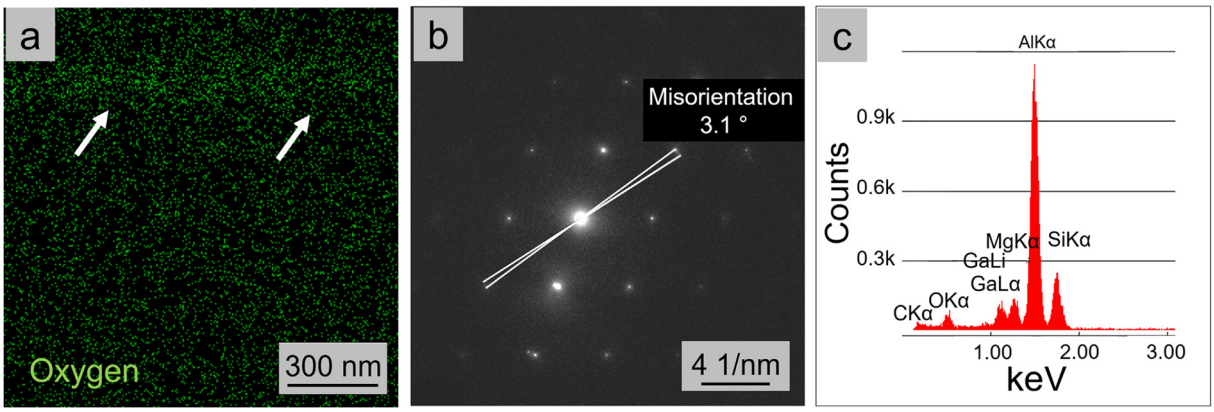

Fig. 10. Analysis performed on the TEM slices for microstructural characterisation; a) EDX map of oxygen on a TEM lamella revealing a higher oxygen content in the surface-near volume (top) compared to the bulk (border denoted by the white arrows); b) results for SAED performed at positions * and # in Fig. 9 (4-3 b), showing a misorientation of 3.1° between the two areas, thus clearly indicating two adjacent sub grain structures; c) EDX spectrum obtained from the particle ③ in the lamella through the indent 4-3 b in Fig. 9.

Table 3
Results of quasi-static nanoindentation: hardness and reduced elastic modulus (mean ± standard deviation) from 300 measurements in the α-Al-matrix (P_{max} = 1000 μN) and 50 measurements in the eutectic Si-phase (P_{max} = 5000 μN).

	H (GPa)	E_r (GPa)
α-Al-matrix	1.0 ± 0.1	83.6 ± 4.6
Eutectic Si	11.2 ± 1.5	129.5 ± 12.5

Our quasi-static nanoindentation hardness results (1.0 ± 0.1 GPa) for the α-Al-matrix show values that are only slightly lower than values reported for a nickel coated AlSi7Mg0.3 hybrid foam by Jung et al. (2015) [22]. The slightly higher values that they report for the matrix (1.4 ± 0.1 GPa) might be due to the lower indentation force of their experiment (500 μN) or a different manufacturing process of the foam that they used. Those authors also studied the hardness values for the Si phase using the same indentation force as we used in our study (5000 μN). They report a value of 10.3 ± 0.4 GPa, which corresponds well with our own results (11.2 ± 1.5 GPa). Importantly, both previous and our own measurements reveal some variance over the indented surface which we attribute to locally varying microstructure. Specifically, the sub-surface microstructure, Si- or IMP-particles, will influence the deformation resistance and hence the indenter imprint. Our TEM observations around an example quasi-static indent clearly show an interaction of the indent with the Si-particles that hinder dislocation movements into deeper parts of the specimen (see Fig. 8c).

The variations in the local properties affecting the quasi-static indentations naturally also affect the cyclic loading experiments. During the onset of loading, we see a clear influence of the applied load on the indentation depth, in addition to the variation caused by the microstructure. With increasing numbers of cycles, the differences between indents no longer uniquely correspond to differences in the applied load. This is seen by the average maximum depth values. Specifically, some of the indents with lower loads showed higher indentation depths whereas other indents with higher loads showed lower indentation depths. These differences can only be explained by local variations in microstructure that take control over the deformation processes with increasing numbers of cycles. These observations are mirrored by the dimensions and morphology of the pile-up of these indents. Small cyclic indents with very little pile-up and no steps (type S, Fig. 6) are usually observed in areas with no or only few, very small Si-particles. Smaller indent sizes in the advanced regime suggest a relatively high resistance to cyclic plastic deformation with pronounced cyclic hardening. Unexpectedly, when the volume beneath the indent contains hard secondary phases often larger imprints are seen (types M, L, P, Fig. 6). A possible explanation is the release of tensile residual stresses in the Al-matrix coupled with reduction of compressive residual stresses in the Si-particles. We propose that residual stresses arising during cooling after casting due to differences in the thermal shrinkage of the main phases ($\alpha_{th,Al} \cong 2 \cdot \alpha_{th,Si}$) decrease the energy necessary for dislocation slippage in the Al-matrix. It has been shown for quasi-static indentation that residual stresses strongly influence the amount of pile-up [35].

We note that, with increasing indent size, the pile-up volume increases. We propose that blockage of dislocation motion into deeper areas beneath the surface leads to excessive material being pushed out above the surface. Evidence for this is seen in TEM images where dislocations are often not seen in regions below Si-particles (see Fig. 9). Further work is needed to fully clarify the exact mechanisms involved in these processes.

The final resulting cyclic-indentation imprint is influenced by both the plastic strain history and by the extent of strain hardening. We see two very different outcomes for the pure α-Al-matrix:

- There are cases where we observe an early onset of strain hardening. This is seen by a pronounced decrease in $\Delta D_{min\text{-}norm}$ and increase in D_{min}/D_{max} in the incipient regime, and plateaus or negligible changes of both curves in the advanced regime. Ultimately, this leads to small indent imprints with small pile-up (4-2 a, 4-2 b).
- In other cases (5-1 a, 5-3 a), the strain hardening rate appears to be lower, indicated by a slower decrease in $\Delta D_{min\text{-}norm}$ up to about N ~ 20,000 and a decrease in D_{min}/D_{max} in the advanced regime. Repeated indentation leads to significant plastic deformation, larger indents and larger pile-up.

Table 4
Results of quasi-static nanoindentation: hardness and reduced elastic modulus (mean ± standard deviation) measured in the α-Al-matrix with increasing distance to Si-particles, from 10 "lines" placed in the same way as the example indicated in Fig. 2 iii).

Lateral distance (μm)	H (GPa)	E_r (GPa)
0	0.9 ± 0.1	79.9 ± 3.2
5	1.0 ± 0.1	68.9 ± 7.1
10	0.9 ± 0.1	68.4 ± 5.8
15	0.9 ± 0.1	66.6 ± 4.2
20	1.0 ± 0.2	70.3 ± 4.9

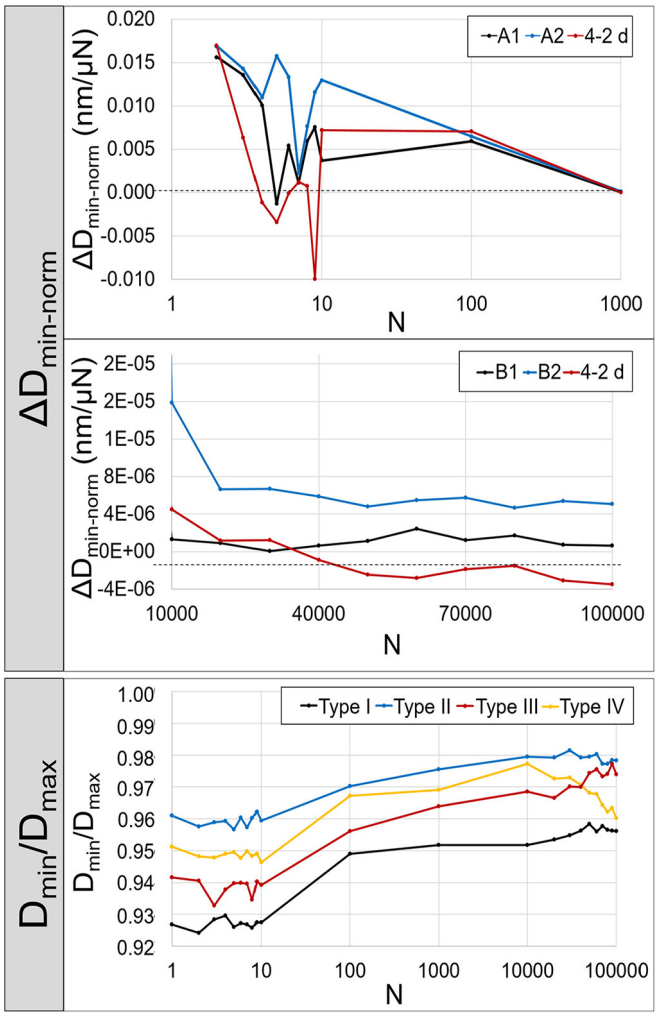

Fig. 11. Typical examples of $\Delta D_{min\text{-}norm}$-N-curves in the "incipient regime" ($N \leq 10^3$), $\Delta D_{min\text{-}norm}$-N-curves in the "advanced regime" ($N \geq 10^4$), and D_{min}/D_{max}-N-curves.

The appearance of pile-up in an initially soft, ductile material merits further consideration. Repeated loading cycles lead to hardening of the affected volume due to repeated activation of dislocations, dislocation multiplication and, eventually, the development of dislocation structures. Subsequently, dislocation motion takes place with plastic deformation propagating into neighbouring volumes. Thus, the material volume affected by indentation increases with increasing cycle number. In this way initially soft volumes, able to accommodate relatively large plastic deformation, become hardened and continuous indentation results in an increase in pile-up. It is worth mentioning, that literature reports of quasi-static nanoindentation experiments on strain-hardened metals found more pile-up as compared to indentations performed in the soft states [36–38]. In those works, however, the indent sizes were smaller. In contrast, under our cyclic loading conditions, higher pile-up correlates with bigger indent sizes. The reason must be that we initially indent a soft material and hardening develops during thousands of loading cycles. Similar observations have been reported for fatigue of a cast AlSiMg alloy with large dendrites. The authors remark that large dendrite cells with tight interdendritic spaces behave like single grains, and that the blocking of dislocations at the boundaries between the dendrite and the eutectic leads to large plastic deformations in these areas. We deduce that in this way hardening can be combined with large amounts of plasticity [39].

An explanation for the differences in the amount of pile-up for similar microstructures might be the orientation of the indenter with respect to the α-Al-dendrite. Correspondingly, if the preferred slip systems in the Al-crystal are oriented such that they experience the highest shear stress during indentation, plastic deformation is extensive. The influence of dendrite orientation on the development of pile-up and of sub grain structures is nicely demonstrated by indent 4-3 e where we cyclically loaded a volume with a dendrite border. While one dendrite clearly shows sub grain structures, the other dendrite exhibits a very low dislocation density. For quasi-static nanoindentation it is well known that the pile-up strongly correlates with the orientation of the slip systems, hence the crystallographic orientation [40,41]. Detailed investigations of the relation between dendrite orientation and the cyclic indentation behaviour are a topic of ongoing work and beyond the scope of this paper.

Larger indents and pile-up come with an increased appearance of steps both in the pile-up material and on the exposed faces of the indents. We assume that these are fatigue slip lines because of their typical morphology. Such steps emerge as a result of dislocation based cyclic plastic deformation in the affected volume. In some areas, extensive localised deformation leads to high peaks in the pile-up. The occurrence of the slip lines does not correlate with the development of sub grain boundaries and a dislocation cell structure. We therefore assume that the slip lines are not associated with persistent slip band formation.

The cyclic deformation curves contain information that provides additional insights into how the final indent morphology is reached. All indents exhibit pronounced plastic deformation at the beginning of loading and a subsequent hardening trend. This is seen in the overall decrease in $\Delta D_{min\text{-}norm}$ and increase in D_{min}/D_{max} followed by constant saturation values or by additional changes emerging at a much lower rate. The hardening is not continuous: relatively large spikes are seen in the $\Delta D_{min\text{-}norm}$-N-curves revealing alternating softening and hardening of the material around the indenter tip. Such pronounced fluctuations are seen for nearly all cyclically loaded specimens at the onset of the experiments. Additional fluctuations are seen in the advanced cycle regime for many of the samples albeit with a smaller amplitude. The lower amplitudes for higher cycle numbers have two very different explanations: spikes are either not visible due to averaging across many indentation cycles or the material approaches a saturation fatigue state.

We hypothesize that some spikes/fluctuations are caused by the release of residual stresses from the Si-inclusions during cyclic loading. Usually, indents showing more pronounced fluctuations in the advanced regime are those placed in regions with Si in the volume below the indent. The fluctuations of $\Delta D_{min\text{-}norm}$ and specifically, fluctuations to negative values, suggest that pushing-out of the indenter takes place. We also see a cross-over of some hysteresis loops, with an unexpected large decrease in the displacement during unloading (data not shown). Similar observations regarding the interactions of residual stresses with the nanoindentation results have been reported for quasi-static loading [35]. Those authors found that the extent of residual stresses correlated with the ratio of the final depth after unloading to the maximum depth reached during one loading event.

Generally, indents in pure Al (4-2 a, 4-2 b, 5-1 a, 5-3 a) exhibit pronounced hardening in the incipient regime (A1), but they differ regarding the advanced regime. Indents 4-2 a and 4-2 b enter a pronounced saturation state while indents 5-1 a and 5-3 a harden with a slower rate and exhibit more fluctuations in the $\Delta D_{min\text{-}norm}$-N-curves. These differences between indents correlate with the indent and pile up sizes. The higher capability of plastic deformation of the two latter indents correlates with the decrease in D_{min}/D_{max} during much of the advanced regime (N ~ 30,000 to 90,000, note the logarithmic scale). More pronounced fluctuations are seen for indents placed on surfaces with Si- or IMP-particles in the volume beneath the indents which we assign to the release of residual stresses. Indents in such regions also differ regarding their hardening behaviour. For example, indent 4-1 a, shows significant hardening in the incipient regime (type A1), just like the

Table 5
Types of cyclic deformation behaviour of the indents: two regions of numbers of cycles have been evaluated separately for the $\Delta D_{min\text{-}norm}$ curves, the "incipient regime" with $N \leqq 10^3$, and the "advanced regime" with $N \geqq 10^4$. For each regime, the curves could be clustered in two groups: A1: lower spikes; A2: higher spikes with overall hardening; B1: saturation; B2: further hardening with lower rate, fluctuations. Indent 4–2 d no group - special curves with pronounced spikes and negative values. For the courses of D_{min}/D_{max} versus the number of cycles, four different types of behaviour were distinguished: I: initial increase, followed by saturation, fluctuations; II: steady increase, more pronounced fluctuations; III: as II, but even more pronounced; IV: increase followed by decrease over the last ~50,000 cycles.

Indent	$\Delta D_{min\text{-}norm}$ "incipient regime"	$\Delta D_{min\text{-}norm}$ "advanced regime"	D_{min}/D_{max}
4-1 a	A1	B1	I
4-2 a	A1	B1	I
4-2 b	A1	B1	I
4-2 d	–	–	IV
4-3 a	A2	B2	II
4-3 b	A2	B2	II
4-3 c	A2	B2	II
4-3 d	A2	B2	II
4-3 e	A2	B2	II
5-1 a	A2	B2	IV
5-1 d	A2	B2	II
5-3 a	A1	B2	IV
5-3 d	A1	B2	III
7-4 c	A2	B2	III

pure Al-indents. The significant amounts of Si-particles in the vicinity of the indent correlate with the further progression of the cyclic deformation curves and a higher pile-up.

We see dislocation cells as predominant dislocation structures in the Al-matrix. Interestingly, dislocation cells have also been identified as main fatigue induced dislocation structures during multiaxial fatigue of A356 bulk materials [39,42]. In those works, the authors note that the cell formation and the extent to which they develop strongly depend on the exact loading path and hence the precise stress conditions [39], as well as on the strain amplitude [42].

We clearly pick up the influence of the secondary phases on the dislocation movement and the cyclic deformation behaviour, even though we indent the matrix extremely locally, with an interaction volume in the range of 10 μm diameter. Si-particles in the volume affected by cyclic indentation clearly hinder the dislocation movement. By confining the available volume, dislocation cells seem to develop earlier in the fatigue process. The mechanism is schematically summarised in Fig. 12 a. In cases with no Si-particles in the vicinity of the indent as shown in Fig. 12 b, we observe a high dislocation density, homogeneously distributed in the volume beneath the indent (4–3 a). If Si-particles are present we see the formation of dislocation cells above the particle, and a very low dislocation density below the particle (4–3 b). We conclude that the microstructural fatigue response is a complex function of the multiaxial loading state, the local microstructure with or without hard precipitates, and the relative orientation of the indenter and the α-Al-dendrite.

5. Conclusions

We investigated the influence of the microstructure on the nanoindentation behaviour of open-cell A356.0 foam struts under quasi-static and cyclic loading conditions. Our findings lead to the following main conclusions:

1. Local variations in microstructure strongly influence the measured quasi-static and cyclic indentation data as well as the indent and the pile-up size and morphology. Indent size after cyclic loading correlates with the pile-up volume.
2. Our quasi-static investigations proved an interaction distance of the Si-particles of 5 μm. The interaction volume during cyclic loading seems to be bigger, in the range of up to 10 μm, where Si- and IMP-particles significantly influence the cyclic deformation behaviour of the matrix.
3. We observed slip bands after cyclic loading in many indent imprints, in both the pile-up and on the indent faces. The extent of slip band formation (size and density) strongly depends on the local microstructure in the volume affected by the indentation.
4. Si-particles act as barriers for the dislocation movement. Under fatigue conditions, they favour the formation of dislocation cells. The formation of the dislocation structures further strongly depends on the dendrite orientation. Interestingly, the pile-up volume and the formation of slip bands in the pile-up does not correlate with the formation of dislocation cells beneath the indent.

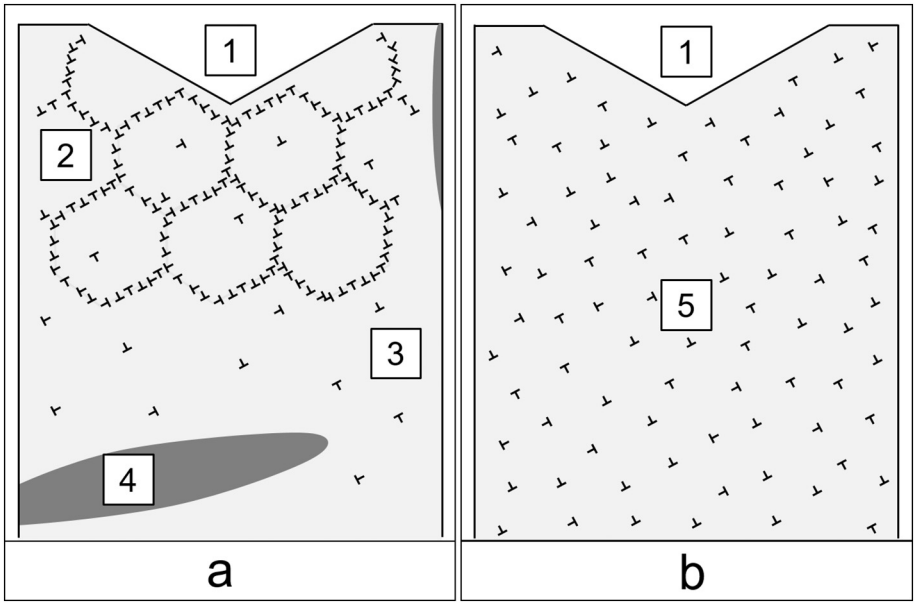

Fig. 12. Schematic illustration of the dislocation distribution and dislocation structures in the volume below the indent a) affected by Si-particle and b) surrounded by the homogeneous α-Al-matrix only. (1 = indent, 2 = high dislocation density and dislocation cells, 3 = low dislocation density, 4 = Si-particle, 5 = high dislocation density, dislocations homogeneously distributed).

5. Importantly, the fatigued volumes below the indents seem to reach different fatigue states, depending on the local microstructure.
6. The results well coincide with observations during fatigue of the bulk alloy reported in the literature. They are therefore an ideal basis for the future development of models predicting the fatigue behaviour of A356.0 open-cell foams.

Our insights into the influence of microstructure on the local cyclic deformation behaviour will help to tailor the fatigue properties to specific applications, for example by using heat treatments or by adding modifiers, thereby changing the distribution, size and morphology of secondary phases. Another important aspect is the relation between dendrite orientation and the cyclic indentation behaviour. Further work is needed to fully elucidate these topics.

Supplementary data to this article can be found online at https://doi.org/10.1016/j.matdes.2020.109016.

Declaration of Competing Interest

The authors declare that they have no known competing financial interests or personal relationships that could have appeared to influence the work reported in this paper.

Acknowledgement

The authors thank Prof. Andreas Bührig-Polaczek and Dr. Sebastian Fischer, Foundry Institute of RWTH Aachen University, for sample casting and fruitful collaborations within SPP 1420, funded by the DFG. We further thank Martina Schaube and Ralf Engelmayer (Materials Science & Engineering, Technische Universität Berlin) for metallographic and specimen preparation, Dr. Dirk Berger and Sören Selve (Central Electron Microscopy Unit ZELMI, Technische Universität Berlin) for HR-SEM, FIB preparation and TEM, and Ana Prates Soares and Andreia Sousa da Silveira (Restorative and Preventive Dentistry, Charité – Universitätsmedizin Berlin) for their help in PCE-μCT data processing. We thank the Helmholtz Zentrum Berlin for the allocation of synchrotron radiation beamtime and the beamtime scientist Dr. Christian Gollwitzer for his excellent support. We are specifically grateful to Prof. Peter Fratzl and Petra Leibner (Max-Planck-Institute of Colloids and Interfaces, Potsdam-Golm) for technical assistance with the nanoindenter. We acknowledge support by the German Research Foundation and the Open Access Publication Fund of TU Berlin.

References

[1] J. Banhart, Aluminum foams: on the road to real applications, MRS Bull. 28 (4) (2003) 290–295, https://doi.org/10.1557/mrs2003.83.
[2] M. Ashby, T. Evans, N.A. Fleck, Metal Foams: A Design Guide, Elsevier, Burlington, 2000.
[3] A. Bührig-Polaczek, et al., Biomimetic cellular metals—using hierarchical structuring for energy absorption, Bioinspir. Biomim. 11 (4) (2016) 45002, https://doi.org/10.1088/1748-3190/11/4/045002.
[4] J. Zhou, Z. Gao, A.M. Cuitino, W.O. Soboyejo, Fatigue of As-fabricated open cell aluminum foams, J. Eng. Mater. Technol. 127 (1) (2005) 40, https://doi.org/10.1115/1.1836770.
[5] J. Zhou, W.O. Soboyejo, Compression–compression fatigue of open cell aluminum foams: macro−/micro- mechanisms and the effects of heat treatment, Mater. Sci. Eng. A 369 (1–2) (2004) 23–35, https://doi.org/10.1016/j.msea.2003.08.009.
[6] A.-M. Harte, N.A. Fleck, M.F. Ashby, Fatigue failure of an open cell and a closed cell aluminium alloy foam, Acta Mater. 47 (8) (1999) 2511–2524, https://doi.org/10.1016/S1359-6454(99)00097-X.
[7] A.C. Kaya, P. Zaslansky, A. Nikolaus, C. Fleck, Tensile failure observations in sintered steel foam struts revealed by sub-micron contrast-enhanced microtomography, Mater. Des. 105 (2016) 190–200, https://doi.org/10.1016/j.matdes.2016.05.069.
[8] P. Schüler, R. Frank, D. Uebel, S.F. Fischer, A. Bührig-Polaczek, C. Fleck, Influence of heat treatments on the microstructure and mechanical behaviour of open cell AlSi7Mg0.3 foams on different lengthscales, Acta Mater. 109 (2016) 32–45, https://doi.org/10.1016/j.actamat.2016.02.041.
[9] S.F. Fischer, P. Schüler, C. Fleck, A. Bührig-Polaczek, Influence of the casting and mould temperatures on the (micro)structure and compression behaviour of investment-cast open-pore aluminium foams, Acta Mater. 61 (14) (2013) 5152–5161, https://doi.org/10.1016/j.actamat.2013.04.069.
[10] A. C. Kaya et al., "High Resolution Synchrotron Tomography Evaluation of the Microstructure/Failure-relationships in Precision Cast AlSi7Mg0.3 Open-cell Foam Struts," (under revision).
[11] X. Zhu, A. Shyam, J. Jones, H. Mayer, J. Lasecki, J. Allison, Effects of microstructure and temperature on fatigue behavior of E319-T7 cast aluminum alloy in very long life cycles, Int. J. Fatigue 28 (11) (2006) 1566–1571, https://doi.org/10.1016/j.ijfatigue.2005.04.016.
[12] S.-W. Han, K. Katsumata, S. Kumai, A. Sato, Effects of solidification structure and aging condition on cyclic stress–strain response in Al–7% Si–0.4% Mg cast alloys, Mater. Sci. Eng. A 337 (1–2) (2002) 170–178, https://doi.org/10.1016/S0921-5093(02)00004-7.
[13] X.-S. Jiang, G.-Q. He, B. Liu, S.-J. Fan, M.-H. Zhu, Microstructure-based analysis of fatigue behaviour of Al-Si-Mg alloy, Trans. Nonferrous Metals Soc. China 21 (3) (2011) 443–448, https://doi.org/10.1016/S1003-6326(11)60734-6.
[14] G.M. Pharr, W.C. Oliver, Measurement of thin film mechanical properties using nanoindentation, MRS Bull. 17 (07) (1992) 28–33, https://doi.org/10.1557/S0883769400041634.
[15] R. Saha, W.D. Nix, Effects of the substrate on the determination of thin film mechanical properties by nanoindentation, Acta Mater. 50 (1) (2002) 23–38, https://doi.org/10.1016/S1359-6454(01)00328-7.
[16] Z. Shan, S.K. Sitaraman, Elastic–plastic characterization of thin films using nanoindentation technique, Thin Solid Films 437 (1–2) (2003) 176–181, https://doi.org/10.1016/S0040-6090(03)00663-1.
[17] J. Němeček, V. Kralik, Local mechanical characterization of metal foams by nanoindentation, KEM 662 (2015) 59–62, https://doi.org/10.4028/www.scientific.net/KEM.662.59.
[18] J. Němeček, V. Králík, J. Vondřejc, A two-scale micromechanical model for aluminium foam based on results from nanoindentation, Comput. Struct. 128 (2013) 136–145, https://doi.org/10.1016/j.compstruc.2013.07.007.
[19] M.A. Hasan, A. Kim, H.-J. Lee, Measuring the cell wall mechanical properties of Al-alloy foams using the nanoindentation method, Compos. Struct. 83 (2) (2008) 180–188, https://doi.org/10.1016/j.compstruct.2007.04.016.
[20] M.A. Hasan, An improved model for FE modeling and simulation of closed cell Al-alloy foams, Adv. Mater. Sci. Eng. 2010 (i) (2010) 1–12, https://doi.org/10.1155/2010/567390.
[21] A.E. Markaki, T.W. Clyne, The effect of cell wall microstructure on the deformation and fracture of aluminium-based foams, Acta Mater. 49 (9) (2001) 1677–1686, https://doi.org/10.1016/S1359-6454(01)00072-6.
[22] A. Jung, Z. Chen, J. Schmauch, C. Motz, S. Diebels, Micromechanical characterisation of Ni/Al hybrid foams by nano- and microindentation coupled with EBSD, Acta Mater. 102 (2016) 38–48, https://doi.org/10.1016/j.actamat.2015.09.018.
[23] Z. Chen, A. Jung, S. Heinze, A. Düster, S. Diebels, Characterization of Ni/Al hybrid foam from atomic to microscale, Proc. Appl. Math. Mech. 15 (1) (2015) 283–284, https://doi.org/10.1002/pamm.201510132.
[24] N.H. Faisal, et al., Cyclic nanoindentation and nano-impact fatigue mechanisms of functionally graded TiN/TiNi film, Shap. Mem. Superelastic. 3 (2) (2017) 149–167, https://doi.org/10.1007/s40830-017-0099-y.
[25] P. Cavaliere, Cyclic deformation of ultra-fine and nanocrystalline metals through nanoindentation: similarities with crack propagation, Proc. Eng. 2 (1) (2010) 213–222, https://doi.org/10.1016/j.proeng.2010.03.023.
[26] S. Jain, A. Gokhale, J. Jain, S.S. Singh, K. Hariharan, Fatigue behavior of aged and solution treated AZ61 Mg alloy at small length scale using nanoindentation, Mater. Sci. Eng. A 684 (2017) 652–659, https://doi.org/10.1016/j.msea.2016.12.111.
[27] B. Xu, Z. Yue, X. Chen, An indentation fatigue depth propagation law, Scr. Mater. 60 (10) (2009) 854–857, https://doi.org/10.1016/j.scriptamat.2009.01.027.
[28] B. Blinn, D. Görzen, M. Klein, D. Eifler, T. Beck, PhyBaLCHT – influence of indentation force on the results of cyclic hardness tests and investigations of comparability to uniaxial fatigue loading, Int. J. Fatigue 119 (2019) 78–88, https://doi.org/10.1016/j.ijfatigue.2018.09.025.
[29] W.C. Oliver, G.M. Pharr, An improved technique for determining hardness and elastic modulus using load and displacement sensing indentation experiments, J. Mater. Res. 7 (06) (1992) 1564–1583, https://doi.org/10.1557/JMR.1992.1564.
[30] W.C. Oliver, G.M. Pharr, Measurement of hardness and elastic modulus by instrumented indentation: advances in understanding and refinements to methodology, J. Mater. Res. 19 (01) (2004) 3–20, https://doi.org/10.1557/jmr.2004.19.1.3.
[31] D. Nečas, P. Klapetek, Gwyddion: an open-source software for SPM data analysis, Open Phys. 10 (1) (2012) 99, https://doi.org/10.2478/s11534-011-0096-2.
[32] J. Schindelin, et al., Fiji: an open-source platform for biological-image analysis, Nat. Methods 9 (7) (2012) 676–682, https://doi.org/10.1038/nmeth.2019.
[33] D. Bartholomew, Polynomial Surface Fit, [Online]. Available: https://imagej.nih.gov/ij/plugins/polynomial-fit/index.html (accessed: May 28 2020).
[34] V. Domnich, Y. Gogotsi, S. Dub, Effect of phase transformations on the shape of the unloading curve in the nanoindentation of silicon, Appl. Phys. Lett. 76 (16) (2000) 2214–2216, https://doi.org/10.1063/1.126300.
[35] M.K. Khan, M.E. Fitzpatrick, S.V. Hainsworth, L. Edwards, Effect of residual stress on the nanoindentation response of aerospace aluminium alloys, Comput. Mater. Sci. 50 (10) (2011) 2967–2976, https://doi.org/10.1016/j.commatsci.2011.05.015.
[36] A. Barnoush, M.T. Welsch, H. Vehoff, Correlation between dislocation density and pop-in phenomena in aluminum studied by nanoindentation and electron channeling contrast imaging, Scr. Mater. 63 (5) (2010) 465–468, https://doi.org/10.1016/j.scriptamat.2010.04.048.
[37] J.D. Gale, A. Achuthan, The effect of work-hardening and pile-up on nanoindentation measurements, J. Mater. Sci. 49 (14) (2014) 5066–5075, https://doi.org/10.1007/s10853-014-8213-4.
[38] H. Biermann, L. Krüger, Moderne Methoden der WerkstoffprüFung, Wiley, 2014.

[39] D.F. Mo, G.Q. He, D.F. Liu, Z.Y. Zhu, Fatigue characteristic and dislocation substructure of A356 casting alloy under multi-axial cyclic loadings, AMR 306–307 (2011) 489–495, https://doi.org/10.4028/www.scientific.net/AMR.306-307.489.

[40] Y. Wang, D. Raabe, C. Klüber, F. Roters, Orientation dependence of nanoindentation pile-up patterns and of nanoindentation microtextures in copper single crystals, Acta Mater. 52 (8) (2004) 2229–2238, https://doi.org/10.1016/j.actamat.2004.01.016.

[41] H.G.M. Kreuzer, R. Pippan, Discrete dislocation simulation of nanoindentation: indentation size effect and the influence of slip band orientation, Acta Mater. 55 (9) (2007) 3229–3235, https://doi.org/10.1016/j.actamat.2007.01.021.

[42] X.-S. Jiang, G.-Q. He, B. Liu, Z.-Y. Zhu, W.-H. Zhang, Fatigue characteristics and microcosmic mechanism of Al-Si-Mg alloys under multiaxial proportional loadings, Int. J. Miner. Metall. Mater. 18 (4) (2011) 437–443, https://doi.org/10.1007/s12613-011-0459-0.